Multifunctional three-dimensional macroporous nanoelectronic networks for smart materials

Jia Liu[a,1], Chong Xie[a,1], Xiaochuan Dai[a,1], Lihua Jin[b], Wei Zhou[a], and Charles M. Lieber[a,b,2]

[a]Department of Chemistry and Chemical Biology, and [b]School of Engineering and Applied Sciences, Harvard University, Cambridge, MA 02138

Seamless and minimally invasive integration of 3D electronic circuitry within host materials could enable the development of materials systems that are self-monitoring and allow for communication with external environments. Here, we report a general strategy for preparing ordered 3D interconnected and addressable macroporous nanoelectronic networks from ordered 2D nanowire nanoelectronic precursors, which are fabricated by conventional lithography. The 3D networks have porosities larger than 99%, contain approximately hundreds of addressable nanowire devices, and have feature sizes from the 10-μm scale (for electrical and structural interconnections) to the 10-nm scale (for device elements). The macroporous nanoelectronic networks were merged with organic gels and polymers to form hybrid materials in which the basic physical and chemical properties of the host were not substantially altered, and electrical measurements further showed a >90% yield of active devices in the hybrid materials. The positions of the nanowire devices were located within 3D hybrid materials with ∼14-nm resolution through simultaneous nanowire device photocurrent/confocal microscopy imaging measurements. In addition, we explored functional properties of these hybrid materials, including (*i*) mapping time-dependent pH changes throughout a nanowire network/agarose gel sample during external solution pH changes, and (*ii*) characterizing the strain field in a hybrid nanoelectronic elastomer structures subject to uniaxial and bending forces. The seamless incorporation of active nanoelectronic networks within 3D materials reveals a powerful approach to smart materials in which the capabilities of multifunctional nanoelectronics allow for active monitoring and control of host systems.

smart systems | field-effect transistor | sensor

Seamlessly merging functional electronic circuits in a minimally invasive manner with host materials in 3D could serve as a pathway for creating "very smart" systems, because this would transform conventional inactive materials into active systems. For example, embedded electronic sensor circuitry could monitor chemical, mechanical, or other changes throughout a host material, thus providing detailed information about the host material's response to external environments as well as desired feedback to the host and external environment (1, 2). Seamless and minimally invasive integration of electronics in 3D has not been achieved, except for our recent example of synthetic tissues (2). Though focused on biological systems, this previous work provides key constraints for achieving our goal of a general strategy for integration electronic networks with host materials, as follows. First, the addressable electronic networks must be macroporous, not planar, to enable 3D interpenetration with the host materials. Second, to minimize invasiveness of the macroporous electronic network it must have (*i*) microscale-to-nanoscale feature sizes, (*ii*) a small filling fraction with respect to the host (e.g., ≤1%), (*iii*) comparable or softer mechanical properties than the host, and (*iv*) an inert chemical response within the host material.

The constraints outlined above require the utilization of 3D nanoelectronic networks that are macroporous and have active elements (nanodevices). Two basic methods have been used to fabricate 3D integrated electronic circuits: the first involves bonding substrates, each containing devices/circuits integrated in 2D, together in a 3D stack (3, 4), and the second exploits bottom-up assembly of nanoelectronic elements in a layer-by-layer manner (5–7). However, both methods yield solid or nonporous 3D structures that only allow the topmost layer of electronic elements to be merged directly with a second material thus precluding integration of all of the electronic elements seamlessly with a host material in 3D. Below, we describe a general strategy for 3D integration of electronics with host materials based on regular arrays of addressable nanowire nanoelectronic elements within 3D macroporous nanoelectronic networks, and also show how these networks can be used to map chemical and mechanical changes induced by the external environment in 3D.

Results and Discussion

We have focused on a bottom-up approach for realizing 3D macroporous nanoelectronic networks and their incorporation into host materials as outlined schematically in Fig. 1. In this approach, we use functional nanowire nanoelectronic elements (Fig. 1*A*), where variations in composition, morphology, and doping encoded during synthesis (8–14) define diverse functionality including devices for logic and memory (15, 16), sensors (17, 18), light-emitting diodes (10), and energy production and storage (19, 20). The macroporous nanoelectronic network with chosen nanowire elements (Fig. 1*B*) is realized through a combination of nanowire assembly and conventional 2D lithography carried out on a sacrificial substrate (see below); removal of the sacrificial layer yields free-standing and flexible 2D macroporous nanoelectronic networks (Fig. 1*B*). The 2D macroporous nanoelectronic networks are organized into 3D macroporous structures by either self-assembly or directed assembly, and then seamlessly merged within host material samples (Fig. 1*C*) using a solution (or liquid) casting process at or near room temperature.

The key steps involved in the fabrication, 3D organization, and characterization of the macroporous nanoelectronic networks are outlined in Fig. 2 (*Materials and Methods*). First, nanowires were uniaxially aligned by contact printing (6, 21) on the surface of a layer of negative photoresist (SU-8), where the SU-8 was deposited by spin-coating on a Ni sacrificial layer deposited on a carrier substrate (Fig. 2 *A, I*). Second, the SU-8 layer with aligned nanowires was patterned to define a periodic array by photolithography or electron beam lithography, and the excess nanowires on unexposed regions of the SU-8 were removed when the pattern was developed (Fig. 2 *A, II*). The nanowire density and feature size in periodic arrays were chosen such that each element contained on average 1–2 nanowires. Third, a second SU-8 layer was deposited and patterned in a mesh structure by lithography (Fig. 2 *A, III*). This SU-8 mesh serves to interconnect the nanowire/SU-8 periodic features and provides an adjustable
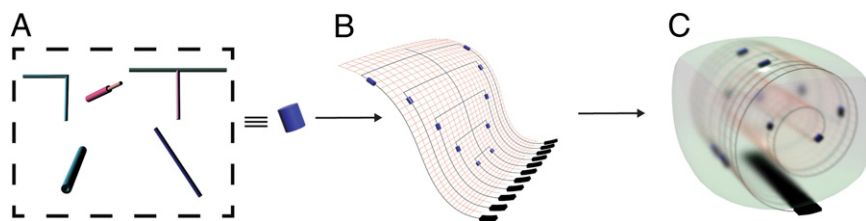
Fig. 1. Strategy for preparing 3D macroporous nanoelectronic networks and integration with host materials. (*A*) Different nanowire nanoelectronic elements (from left to right): kinked nanowire, nanotube, core-shell, straight, and branched nanowire. (*B*) Free-standing 2D macroporous nanowire nanoelectronic precursor. Blue, nanoelectronic element; orange, passivation polymer; black, metal contact and input/output. (*C*) The 3D macroporous nanoelectronic networks integrated with host materials (gray).

support structure to tune the mechanical properties. Fourth, metal interconnects were defined by standard lithography and metal deposition on top of the appropriate regions of the SU-8 mesh, such that the end of nanowires were contacted and the nanowire elements were independently addressable (Fig. 2 *A, IV*). Last, a third SU-8 layer was lithographically patterned to cover and passivate the metal interconnects.

Dark-field optical microscopy images obtained from a typical nanoelectronic mesh fabrication corresponding to the steps described above (Fig. 2 *B, I–IV*) highlight several important features. First, the images recorded after contact printing (Fig. 2 *B, I*) confirm that nanowires are well aligned over areas where nanowire devices are fabricated. We can achieve good nanowire alignment on length scales up to at least several centimeters, as reported elsewhere (6, 21). Second, a representative dark-field image of the patterned periodic nanowire regions (Fig. 2 *B, II*) shows that this process removes nearly all of the nanowires outside of the desired features. Nanowires can be observed to extend outside of the periodic circular feature (i.e., an end is fixed at the feature) at some points; however, these are infrequent and do not affect subsequent steps defining the nanodevice interconnections. Third, images of the underlying SU-8 mesh (Fig. 2 *B, III*) and final device network with SU-8 passivated metal contacts and interconnects (Fig. 2 *B, IV*) highlight the regular array of addressable nanowire devices realized in our fabrication process. Last, SEM images (Fig. 2*C*) show that these device elements have on average 1–2 nanowires in parallel.

The 2D nanoelectronic mesh structures were converted to free-standing macroporous networks by dissolution of the sacrificial Ni layers over a period of 1–2 h (*Materials and Methods*). Representative images of a free-standing nanoelectronic network (Fig. 2 *D* and *E*, Fig. S1) highlight the 3D and flexible characteristics of the structure and show how input/output (I/O) to the free-standing network can be fixed at one end outside of a solution measurement Petri-dish chamber. Electrical characterization of individually addressable nanowire device elements in a free-standing mesh demonstrates that the device yield is typically ~90% (from 128 device design) for the free-standing nanoelectronic mesh structures fabricated in this way. The average conductance of the devices from a representative free-standing mesh (Fig. 2*F*), 2.85 ± 1.6 μS, is consistent with 1–2 nanowires per device based on measurements of similar (30 nm diameter, 2 μm channel length) p-type Si single nanowire devices (22), and thus also agrees with the structural data discussed above. In addition, by varying the printed nanowire density and source/drain (S/D) metal contact widths, it is possible to tune further the average number of nanowires per device element.

These 2D free-standing macroporous nanoelectronic networks were transformed to 3D structures using two general methods. First, 2D macroporous nanoelectronic networks were manually rolled up into 3D arrays (Fig. 2*G*), with nanoelectronic elements in different layers of the resulting "scroll" similar to our previous results for synthetic vascular structures (2). Second, by introducing built-in stress in metal interconnects with a trilayer metal stack

(*Materials and Methods*), the mesh can be designed to self-organize into a similar scrolled structure as achieved by manual rolling. A reconstructed 3D confocal fluorescent image of a 3D nanoelectronic mesh array produced in this manner (Fig. 2*H*) shows clearly the 3D macroporous nanoelectronic network and can be used to estimate a free volume of (>99%). More generally, these self-organized 3D macroporous nanoelectronic structures could be readily diversified to meet goals for different hybrid materials using established mechanical design and bifurcation strategies (23).

Qualitatively, the facile manipulation of the macroporous nanoelectronic networks to form 3D structures suggests a very low effective bending stiffness. We have evaluated the effective bending stiffness, $\overline{D}$, using a combination of calculations and experimental measurements (*SI Text*; Figs. S2 and S3). In short, $\overline{D} = \alpha_s D_s + \alpha_m D_m$, where D_s and D_m are bending stiffness per unit width for the SU-8 structural elements and SU-8/metal/SU-8 interconnects, respectively, and α_s and α_m are the respective area fractions for these elements in the networks. For typical 3D macroporous nanoelectronic networks, the area fraction for both types of elements (i.e., SU-8 and SU-8/metal/SU-8) can range from 1% to 10%, yielding values of the effective bending stiffness from 0.0038 to 0.0378 nN/m.

The semiconductor nanowire elements can display multiple sensory functionalities, including photon (24), chemical, biochemical, and potentiometric (17, 22) as well as strain (25, 26) detection, which make them particularly attractive for preparing hybrid active materials as described below. We have first characterized photoconductivity changes (i.e., photon detection) of nanowire elements while imaging the nanoelectronic networks with a confocal microscope by recording conductance as a function of *xyz* coordinates and overlapping with simultaneously acquired fluorescence images (*Materials and Methods*; Fig. 3*A*; Fig. S4*A*). As the focused laser is scanned across a sample (Fig. 3 *A, I*) an increase of conductance due to the photocurrent (27) in nanowire is recorded at the positions of the nanowire devices. The resolution of this approach can be assessed in two ways. Conventionally, the plot of conductance vs. position (Fig. 3 *A, II*) can be fit with a Gaussian function, and its FWHM reflects the diffraction limited resolution of the illuminating light spot. Second, and recognizing that the nanowire diameter (30 nm) is line-like, we can use methods similar to superresolution imaging technologies (28, 29) to locate the nanowire to much higher precision by identifying the peak position from the Gaussian fit. We note that a similar concept as exploited in stochastic superresolution imaging to resolve close points can be implemented in our photoconductivity maps because individual devices can be turned on and off as needed (28).

A typical high-resolution photoconductivity image of a single nanowire device (Fig. 3 *B, I*) shows clearly the position of the nanowire. The conductance change vs. *x* position perpendicular to the nanowire axis (Fig. 3 *B, II*; Fig. S4*B*) yielded a FWHM of 314 ± 32 nm (*n* = 20) resolution, consistent with confocal microscopy imaging resolution (202 nm) in this experiment. Moreover,
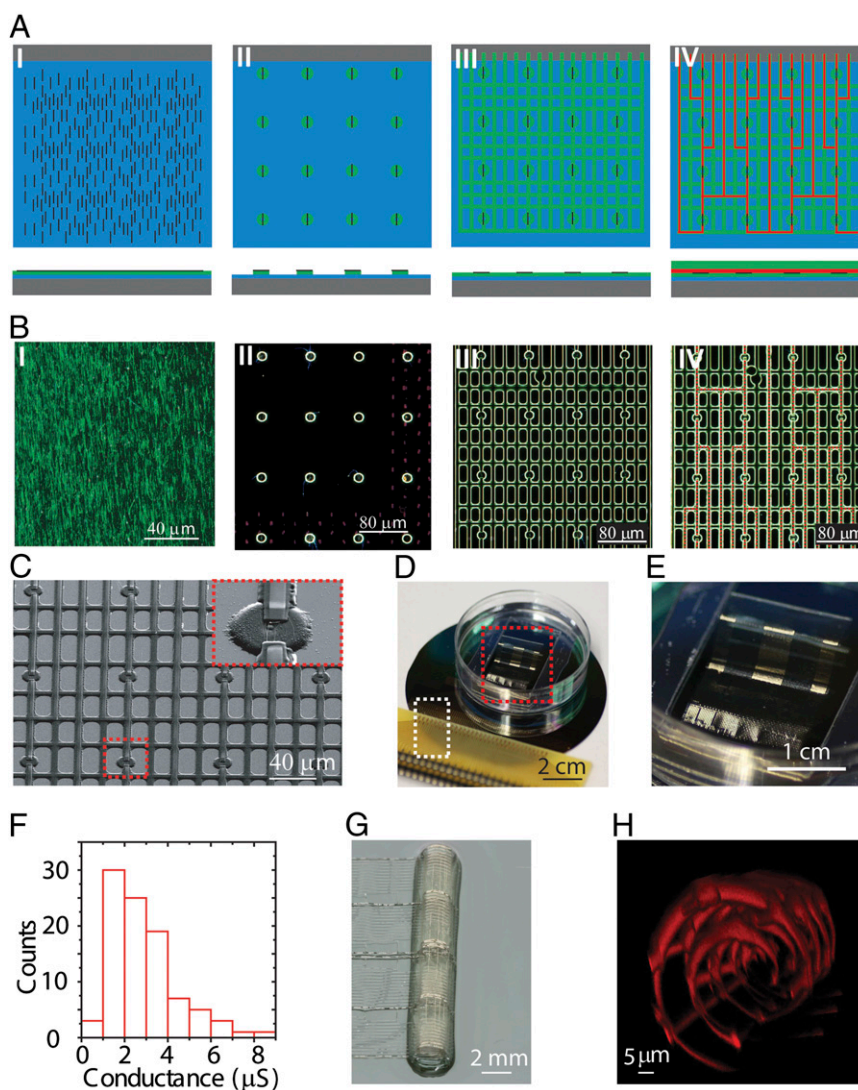
Fig. 2. Organized 2D and 3D macroporous nanoelectronic networks. (*A*) Schematics of nanowire registration by contact printing and SU-8 patterning. Gray, silicon wafer; blue, Ni sacrificial layer; black ribbon, nanowire; green, SU-8; red, metal contact. (*Upper*) Top view. (*Lower*) Side view. (*I*) Contact printing nanowire on SU-8. (*II*) Regular SU-8 structure was patterned by lithography to immobilize nanowires. Extra nanowires were washed away during the development process of SU-8. (*III*) Regular bottom SU-8 structure was patterned by spin-coating and lithography. (*IV*) Regular metal contact was patterned by lithography and thermal evaporation, followed by top SU-8 passivation. (*B*) Dark-field optical images corresponding to each step of schematics in *A*. The nanowire and SU-8 features appear green in these images. The small red features on the right and lower edges of the image in *II* correspond to metal lithography markers used in alignment. The red dashed line highlights metal contacts/interconnects in *IV*. (*C*) SEM image of a 2D macroporous nanoelectronic network before release from the substrate. (*Inset*) Zoom-in of the region enclosed by the small red dashed box containing a single nanowire device. (*D*) Photograph of wire-bonded free-standing 2D macroporous nanoelectronic network in Petri dish chamber for aqueous solution measurements. The red dashed box highlights the free-standing portion of the nanoelectronic network, and the white-dashed box encloses the wire-bonded interface between the input/output and printed circuit board connector board. (*E*) Zoom-in of the region enclosed by the red dashed box in *D*. (*F*) Histogram nanowire device conductance in the free-standing 2D macroporous nanoelectronic networks. (*G*) Photograph of a manually scrolled-up 3D macroporous nanoelectronic network. (*H*) 3D reconstructed confocal fluorescence images of self-organized 3D macroporous nanoelectronic network viewed along the *x*-axis. Nonsymmetrical Cr/Pd/Cr metal layers (*Materials and Methods*), which are stressed, were used to drive self-organization. The SU-8 ribbons were doped with rhodamine 6G for imaging.

nanowire position determined from the peaks of Gaussian fits (Fig. S4*C*) yielded a SD of 14 nm (*n* = 20), and shows that the position of devices can be localized with a precision better than the diffraction limit. In addition, we have acquired simultaneous photoconductivity and fluorescence confocal microscopy images to map the positions of nanowire devices in 3D macroporous nanoelectronic networks. Reconstructed 3D images (Fig. 3*C*) show that the 12 active nanowire devices can be readily mapped with respect to *xyz* coordinated in the rolled-up macroporous nanoelectronic network structure. Given the complexity possible in 3D nanoelectric/host hybrid materials, this approach provides

straightforward methodology for determining at high resolution the positions of the active nanoelectronic sensory elements with respect to structures within the host. In the future, we also note that the resolution could be even further improved by incorporating point-like transistor photoconductivity detectors (17, 30), p-type/n-type (*p-n*) photodiodes (31) and p-type/intrinsic/n-type (*p-i-n*) avalanche photodiodes (32), nanowire building blocks within the 3D macroporous nanoelectronic network.

Second, we have used macroporous nanowire nanoelectronic networks to map pH changes in 3D through agarose gel using a macroporous nanoelectronic/gel hybrid, and for comparison, in
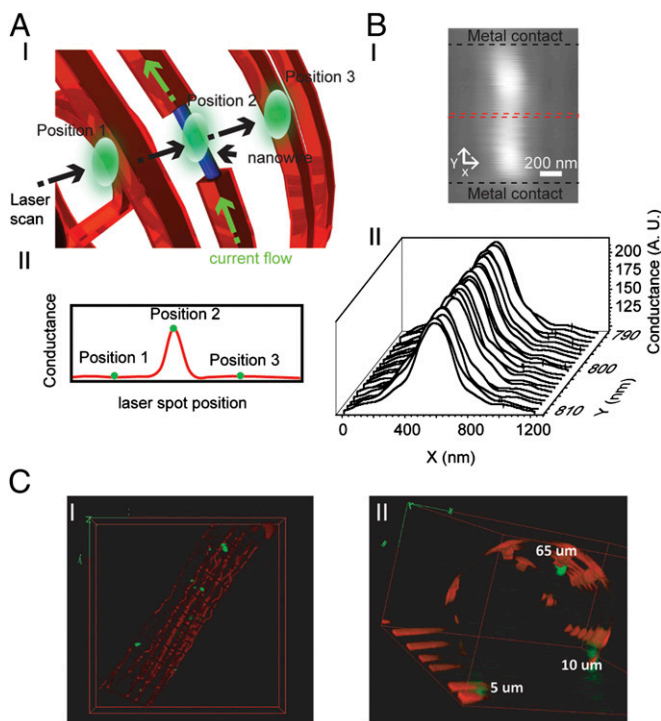
Fig. 3. The 3D macroporous photodetectors and device localization. (*A*) Schematics of the single 3D macroporous nanowire photodetector characterization. Green ellipse, laser spot; blue cylinder, nanowire; orange, SU-8 mesh network. The illumination of the laser spot generated from confocal microscope on the nanowire device (*I*) makes the conductance change of nanowire, which could be (*II*) correlated with laser spot position. Green spots in *II* correlate to the laser spot positions in *I*. (*B*) High-resolution (1 nm per pixel) photocurrent image (*I*) from a single nanowire device (2 μm channel length) on substrate recorded with focused laser spot scanned in *xy* plane. The black dash lines indicate the boundary of metal contact in the device. (*II*) The 20× photocurrent measurements from the central region (red dash box) of the nanowire device with high resolution (the distance for each trace in *x* direction is 1 nm). (*C*) A 3D reconstructed photocurrent imaging overlapped with confocal microscopy imaging shows the spatial correlation between nanowire photodetectors with SU-8 framework in 3D. Green, false color of the photocurrent signal; orange (rhodamine 6G), SU-8 mesh network. Dimensions in *I*, *x*: 317 μm; *y*: 317 μm; *z*: 53 μm; *II*, *x*: 127 μm; *y*: 127 μm; *z*: 65 μm. The white numbers in *II* indicate the heights of the nanowire photodetectors.

aqueous solution using a free-standing 3D nanoelectronic sensory network. The hybrid nanoelectronic/gel material was prepared by casting the agarose around a rolled-up macroporous nanoelectronic network, where the gel and SU-8 mesh of the nanoelectronic network were doped with DAPI and rhodamine 6G, respectively (*Materials and Methods*). A reconstructed 3D confocal microscopy image of the hybrid material (Fig. 4*A*) shows clearly the 3D device mesh fully embedded within an agarose gel block without phase separation. To carry out sensing experiments, either the 3D nanoelectronic/gel hybrid material or a 3D nanoelectronic mesh was contained within a microfluidic chamber (Fig. 4*B*). Positions of nanowire transistor devices, which can function as very sensitive chemical/biological detectors (17, 22, 33), were determined by the photocurrent mapping method described above. For both 3D nanoelectronic mesh and nanoelectronic/gel hybrid, we recorded signals simultaneously from four devices chosen to span positions from upper to lower boundary of mesh or gel, where representative *z*-coordinates of the devices positions within the hybrid sample are highlighted in Fig. 4*C*; a similar *z*-range of devices for the free nanoelectronic mesh was also used.

Representative data recorded from p-type nanowire field-effect transistor (FET) devices in 3D mesh network without gel

(Fig. 4 *D*, *I*) and in the hybrid 3D nanoelectronic mesh/agarose gel hybrid (Fig. 4 *D*, *II*) highlight several important points. First, the device within 3D macroporous network without gel showed fast stepwise conductance changes (<1 s) with solution pH changes. The typical sensitivity of these devices was ∼40 mV/pH, and is consistent with values reported for similar nanowire devices (18). Second, the device within the 3D nanoelectronic mesh/gel hybrid exhibited substantially slower transition times with corresponding changes of the solution pH; that is, signal change required on the order of 2,000 s to reach steady state, and thus was 1,000-fold slower than in free solution. Third, the device within the 3D nanoelectronic mesh/gel hybrid exhibited lower pH sensitivity in terms of mV/pH; that is, 20–40 mV/pH for the device in gel compared with 40–50 mV/pH for the device in free solution.

Direct comparison of the temporal responses of four devices at different 3D positions in the two types of samples (Fig. 4*E*) provides additional insight into the pH changes. The time to achieve one-half pH unit change for the four different devices in 3D macroporous network without gel (Fig. 4 *E*, *I*) is ∼0.5 s, and the difference between devices is only ∼0.01 s. We note that the time delay in the data recorded from device d4 is consistent with the downstream position of this device within the fluidic channel. In contrast, the time to achieve one-half for the four devices in the 3D nanoelectronic mesh/gel hybrid (Fig. 4 *E*, *II*) range from
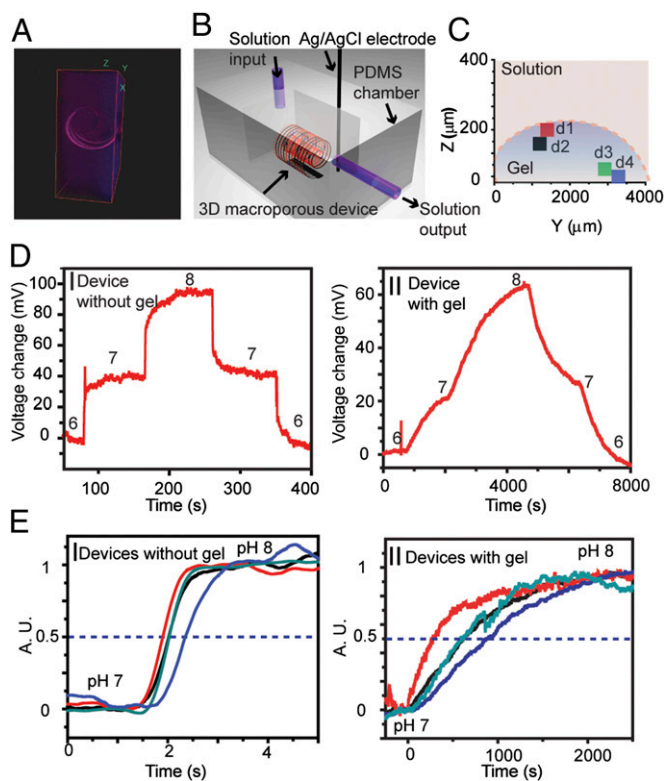
Fig. 4. The 3D macroporous chemical sensors. (*A*) The *xz* views of 3D reconstructed image of the 3D macroporous nanoelectronic network in gel. Red (rhodamine 6G), SU-8 mesh network; blue (DAPI), agarose gel. Dimensions: *x* = 317 μm; *y* = 317 μm; and *z* = 144 μm. (*B*) Schematics of the experimental setup. (*C*) The projection of four nanowire devices in the *yz* plane. Red dashed line corresponds to the approximate gel boundary, and the red and blue areas correspond to aqueous solution and agarose gel, respectively. (*D*) Representative change in calibrated voltage over time with pH change for 3D macroporous nanowire chemical sensors (*I*) in solution and (*II*) embedded in agarose gel. (*E*) Calibrated voltage with one pH value change in solution for four different devices located in 3D space. (*I*) Four devices without gel and (*II*) four devices embedded in agarose gel.

~280 to 890 s for devices d1–d4, respectively (device positions are shown in Fig. 4C). The results show that the device response time within the agarose is ~500–1,700 times slower than in solution and is proportional to the distance from the solution/gel boundary, although the detailed variation suggests heterogeneity in the diffusion within the agarose gel. Significantly, the ability to map the diffusion of molecular and biomolecular species in 3D hybrid systems using the macroporous nanoelectronic sensory networks offers opportunities for self-monitoring of gel, polymers, and tissue systems relevant to many areas of science and technology (34, 35).

Third, we have used embedded 3D macroporous nanoelectronic networks to map strain distributions in elastomeric silicone host materials. Previous studies have shown that Si nanowires have a high piezoresistance response (25), making them good candidates for strain sensors (26). To explore the potential of Si nanowire device arrays to map strain within materials, we have prepared and characterized 3D macroporous nanoelectronic network/elastomer hybrid materials (*Materials and Methods*). The resulting hybrid macroporous nanoelectronic network/elastomer cylinders had volumes of ~300 mm^3 with volume ratio of device to elastomer of <0.1%. X-ray micro-CT studies of the nanoelectronic network/elastomer cylinders (Fig. 5A; Fig. S5) were used to determine the 3D metal interconnects and locations of nanowire devices within the cylindrical hybrid structures (*Materials and Methods*). The alignment of nanowire elements along the cylinder axis was confirmed by dark-field optical microscopy images (Fig. 5B), which show the nanowires lying along the cylinder (z) axis.

The good axial alignment of the nanowire devices was exploited to calibrate the strain sensitivity of each element within the 3D hybrid structure in a pure tensile strain field. Application of a 10% tensile strain along the cylinder axis (Fig. S5A) yielded decreases in conductance up to 200 nS for the individual devices, d1–d11. Because the conductance immediately returned to baseline when strain was released, and under compressive loads the conductance change had the opposite sign, we can conclude that these changes do reflect strain transferred to the nanowire sensors. From the specific response of the devices within the hybrid structure we calculate and assign a calibrated conductance change/1% strain value for each of the 11 sensor elements (Fig. S5), and use this for analysis of different applied strains. For example, we applied a bending strain to the cylinder, and from the recorded conductance changes and calibration values were able to map readily the 3D strain field as shown in Fig. 5C. We note that the one-dimensional geometry of nanowires gives these strain sensors nearly perfect directional selectivity, and thus, by developing a macroporous nanoelectronic network with nanowires devices aligned parallel and perpendicular to the cylinder axis, enables mapping of all three components of the strain field in the future.

Conclusions

We have demonstrated a general strategy for preparing ordered 3D interconnected and addressable macroporous nanoelectronic networks from ordered 2D nanowire nanoelectronic precursors, which are fabricated by conventional lithography. The 3D networks have porosities larger than 99%, contain hundreds of addressable nanowire devices, and have feature sizes from the 10-μm scale for electrical and structural interconnections to the 10-nm scale for the functional nanowire device elements. The macroporous nanoelectronic networks were merged with organic gels and polymers to form hybrid materials in which the basic physical and chemical properties of the host were not substantially altered, and electrical measurements further show >90% yield of active devices in the hybrid materials. We further demonstrated a unique approach to determine the positions of the nanowire devices within 3D hybrid materials with ~14-nm resolution that involves simultaneous nanowire device photocurrent/confocal microscopy imaging measurements. This method also could have substantial impact on localizing device positions in macroporous nanoelectronic/biological samples, where it provides the capability of determining positions of sensory devices at the subcellular level. In addition, we explored functional properties of these hybrid materials. First, we showed that it was possible to map time-dependent pH changes throughout a nanowire network/agarose gel sample during external solution pH changes. These results suggest the substantial promise of 3D macroporous nanoelectronic networks for real-time mapping of diffusion of chemical and biological species through polymeric samples as well as biological materials such as synthetic tissue (34, 36). Second, we demonstrated that Si nanowire elements can function as well-defined strain sensors, and thereby characterize the strain field in hybrid nanoelectronic elastomer structures subject to uniaxial and bending forces. More generally, we believe our approach to fabrication of multifunctional 3D electronics and integration with host materials suggests substantial promise for (i) general fabrication of truly 3D integrated circuits based on conventional fabrication processes via assembly from a 2D precursor, and (ii) seamless 3D incorporation of multifunctional nanoelectronics into living and nonliving systems leading to make very smart material systems and another level of "cyborg" tissues.

Materials and Methods

Nanowire Synthesis. Single crystalline nanowires were synthesized using the Au nanocluster-catalyzed vapor–liquid–solid growth mechanism in a home-built chemical vapor deposition system (*SI Text*) described previously (37).

Three-Dimensional Macroporous Nanoelectronic Networks. Macroporous nanowire nanoelectronic networks were fabricated on the oxide or nitride surfaces of silicon substrates (600 nm SiO$_2$ or 100 SiO$_2$/200 Si$_3$N$_4$, n-type 0.005 V/cm; Nova Electronic Materials). Key steps in fabrication of the 3D nanoelectronic networks were as follows (*SI Text*): (i) lithography and thermal deposition were used to pattern a 100-nm nickel relief layer. (ii) A 300- to 500-nm layer of SU-8 photoresist (2000.5; MicroChem Corp.) was deposited
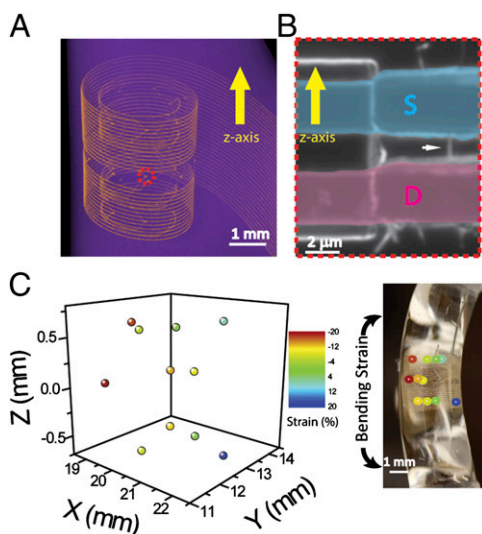
Fig. 5. The 3D macroporous strain sensors embedded in elastomer. (A) Micro-CT 3D reconstruction of the macroporous strain sensor array embedded in a piece of elastomer. Pseudocolors are applied: orange, metal; purple, elastomer. (B) Dark-field microscopy image of a typical nanowire device indicated by red dash circle in A. All of the functional nanowires are intentionally aligned parallel to the axial axis of the elastomer cylinder. The white arrow points to a nanowire. (C) A bending strain field was applied to the elastomer piece. The 3D strain field was mapped by the nanowire strain sensors using the sensitivity calibration of the nanowire devices. The detected strains are labeled in the cylinder image at the device positions.

over the entire chip followed by prebaking at 65 °C and 95 °C for 2 and 4 min, respectively, then (*iii*) synthesized nanowires were directly printed from growth wafer over the SU-8 layer. (*iv*) Lithography was used to define a regular pattern on the SU-8, and after postbaking (65 °C and 95 °C for 2 and 4 min, respectively), the pattern was developed (SU-8 developer; MicroChem Corp.) and cured at 180 °C for 20 min. (*v*) A 300- to 500-nm layer of SU-8 photoresist was deposited, prebaked as above, and then patterned to serve as the lower passivation layer and support for the overall structure. (*vi*) Lithography and thermal deposition were used to define and deposit metal contacts/interconnects for the array, where symmetrical Cr/Pd/Cr (1.5/50–80/1.5 nm) and nonsymmetrical Cr/Pd/Cr (1.5/50–80/50–80 nm) were deposited for the unstressed and self-organized networks, respectively. (*vii*) A 300- to 500-nm layer of SU-8 photoresist was deposited, prebaked as above, and then patterned to define the top SU-8 passivation layer for nanoelectronic network. (*viii*) Macroporous nanowire nanoelectronic networks were released from substrates by nickel etching (Nickel Etchant TFB; Transene Company Inc.) for 60–120 min at 25 °C, and (*ix*) were then dried by a critical point drying (Autosamdri 815 Series A; Tousimis).

Characterization of Macroporous Nanoelectronic Networks. SEM (Zeiss Ultra55/Supra55VP field-emission SEMs) was used to characterize the macroporous nanoelectronic networks. Bright-field and dark-field optical micrographs of samples were acquired on an Olympus FSX100 system (*SI Text*). Fluorescence images of the 3D macroporous nanoelectronic networks were obtained by doping the SU-8 resist with rhodamine 6G (Sigma-Aldrich Corp.). ImageJ (version 1.45i, http://imagej.nih.gov/ij/) was used for image analysis. Mechanical measurements on SU-8/metal/SU-8 ribbons were made using an atomic force microscope and calibrated tip (MFP-3D; Asylum Corp.).

Electrical Measurement of 3D Macroporous Nanoelectronic Networks. Nanowire device recording was carried out with a 100-mV DC source voltage, and the current was amplified with a home-built multichannel current/voltage preamplifier with a typical gain of 10^6 A/V. The signals were filtered through a home-built conditioner with bandpass of 0–3 kHz, digitized at a sampling rate of 20 kHz (Axon Digi1440A), and recorded using Clampex 10 software (MDS Analytical Technologies).

Three-Dimensional Macroporous Photodetectors and Device Localization in 3D. Confocal laser scanning microscopy (FluoView FV1000; Olympus America Inc.) was used to characterize the 3D macroporous nanoelectronic network (*SI Text*). The macroporous nanoelectronic network was immersed into deionized (DI) water; individual devices were biased with 100 mV; and 40× or 100× water-immersion objectives were used for imaging. The conductance signal from the resulting images was read out by ImageJ, and the data were analyzed and fitted by OriginPro.

Three-Dimensional Macroporous Chemical Sensors. Agarose (Sigma) was dissolved into DI water and made as 0.5%, and heated to 100 °C. The gel was drop casted onto the device and cooled to room temperature (*SI Text*). A microfluidic polydimethylsiloxane fluidic chamber with input/output tubing and Ag/AgCl reference electrode was used to deliver different pH solutions (pH 6–8) while recording device response in real time.

Three-Dimensional Nanoelectronic/Elastomer Strain Sensors. A freestanding 2D macroporous nanoelectronic network was suspended in water, placed on a thin (200–500 μm) piece of cured silicone elastomer sheet (Sylgard 184; Dow Corning), rolled into a cylinder, infiltrated with silicone elastomer, and cured. The resulting hybrid nanoelectronic/elastomer cylinders had volumes of ~300 mm³, with a volume ratio of device to elastomer of <0.1%. Structures were characterized by X-ray micro-CT (HMXST225; Nikon Metrology, Inc.). The nanowire piezoelectric response was calibrated under tensile strain (Fig. S5), where the strain was calculated from the length change of the cylindrical hybrid structure. The bending strain field was determined using the calibrated nanowire strain sensors.

1. Reuss RH, Hopper DG, Park JG (2006) Macroelectronics. *MRS Bull* 31(6):447–454.
2. Tian B, et al. (2012) Macroporous nanowire nanoelectronic scaffolds for synthetic tissues. *Nat Mater* 11(11):986–994.
3. Al-sarawi SF, Abbott D, Franzon PD (1998) A review of 3-D packaging technology. *IEEE Trans Comp Pag Manuf Technol* 21(1):2–14.
4. Benkart P, et al. (2005) 3D chip stack technology using through-chip interconnects. *IEEE Des Test Comput* 22(6):512–518.
5. Ahn JH, et al. (2006) Heterogeneous three-dimensional electronics by use of printed semiconductor nanomaterials. *Science* 314(5806):1754–1757.
6. Javey A, Nam S, Friedman RS, Yan H, Lieber CM (2007) Layer-by-layer assembly of nanowires for three-dimensional, multifunctional electronics. *Nano Lett* 7(3):773–777.
7. Nam S, Jiang X, Xiong Q, Ham D, Lieber CM (2009) Vertically integrated, three-dimensional nanowire complementary metal-oxide-semiconductor circuits. *Proc Natl Acad Sci USA* 106(50):21035–21038.
8. Lu W, Lieber CM (2007) Nanoelectronics from the bottom up. *Nat Mater* 6(11):841–850.
9. Lieber CM, Wang ZL (2007) Functional nanowire. *MRS Bull* 32(2):99–104.
10. Qian F, Gradecak S, Li Y, Wen CY, Lieber CM (2005) Core/multishell nanowire heterostructures as multicolor, high-efficiency light-emitting diodes. *Nano Lett* 5(11):2287–2291.
11. Tian B, et al. (2007) Coaxial silicon nanowires as solar cells and nanoelectronic power sources. *Nature* 449(7164):885–889.
12. Tian B, Xie P, Kempa TJ, Bell DC, Lieber CM (2009) Single-crystalline kinked semiconductor nanowire superstructures. *Nat Nanotechnol* 4(12):824–829.
13. Gao R, et al. (2012) Outside looking in: Nanotube transistor intracellular sensors. *Nano Lett* 12(6):3329–3333.
14. Jiang X, et al. (2011) Rational growth of branched nanowire heterostructures with synthetically encoded properties and function. *Proc Natl Acad Sci USA* 108(30):12212–12216.
15. Yan H, et al. (2011) Programmable nanowire circuits for nanoprocessors. *Nature* 470(7333):240–244.
16. Xiang J, et al. (2006) Ge/Si nanowire heterostructures as high-performance field-effect transistors. *Nature* 441(7092):489–493.
17. Cui Y, Wei Q, Park H, Lieber CM (2001) Nanowire nanosensors for highly sensitive and selective detection of biological and chemical species. *Science* 293(5533):1289–1292.
18. Tian B, et al. (2010) Three-dimensional, flexible nanoscale field-effect transistors as localized bioprobes. *Science* 329(5993):830–834.
19. Qin Y, Wang XD, Wang ZL (2008) Microfibre-nanowire hybrid structure for energy scavenging. *Nature* 451(7180):809–813.
20. Chan CK, et al. (2008) High-performance lithium battery anodes using silicon nanowires. *Nat Nanotechnol* 3(1):31–35.
21. Fan ZY, et al. (2008) Wafer-scale assembly of highly ordered semiconductor nanowire arrays by contact printing. *Nano Lett* 8(1):20–25.
22. Zheng G, Patolsky F, Cui Y, Wang WU, Lieber CM (2005) Multiplexed electrical detection of cancer markers with nanowire sensor arrays. *Nat Biotechnol* 23(10):1294–1301.
23. Freund LB (2000) Substrate curvature due to thin film mismatch strain in the nonlinear deformation range. *J Mech Phys Solids* 48(6–7):1159–1174.
24. Fan Z, Ho JC, Jacobson ZA, Razavi H, Javey A (2008) Large-scale, heterogeneous integration of nanowire arrays for image sensor circuitry. *Proc Natl Acad Sci USA* 105(32):11066–11070.
25. He R, Yang P (2006) Giant piezoresistance effect in silicon nanowires. *Nat Nanotechnol* 1(1):42–46.
26. Lee CH, Kim DR, Zheng X (2010) Fabricating nanowire devices on diverse substrates by simple transfer-printing methods. *Proc Natl Acad Sci USA* 107(22):9950–9955.
27. Tsen AW, Donev LAK, Kurt H, Herman LH, Park J (2009) Imaging the electrical conductance of individual carbon nanotubes with photothermal current microscopy. *Nat Nanotechnol* 4(2):108–113.
28. Huang B, Wang WQ, Bates M, Zhuang XW (2008) Three-dimensional super-resolution imaging by stochastic optical reconstruction microscopy. *Science* 319(5864):810–813.
29. Toprak E, Balci H, Blehm BH, Selvin PR (2007) Three-dimensional particle tracking via bifocal imaging. *Nano Lett* 7(7):2043–2045.
30. Cohen-Karni T, et al. (2012) Synthetically encoded ultrashort-channel nanowire transistors for fast, pointlike cellular signal detection. *Nano Lett* 12(5):2639–2644.
31. Jiang Z, Qing Q, Xie P, Gao R, Lieber CM (2012) Kinked p-n junction nanowire probes for high spatial resolution sensing and intracellular recording. *Nano Lett* 12(3):1711–1716.
32. Hayden O, Agarwal R, Lieber CM (2006) Nanoscale avalanche photodiodes for highly sensitive and spatially resolved photon detection. *Nat Mater* 5(5):352–356.
33. Patolsky F, Timko BP, Zheng G, Lieber CM (2007) Nanowire-based nanoelectronic devices in the life science. *MRS Bull* 32(2):142–149.
34. Griffith LG, Swartz MA (2006) Capturing complex 3D tissue physiology in vitro. *Nat Rev Mol Cell Biol* 7(3):211–224.
35. Sanger F, Nicklen S, Coulson AR (1977) DNA sequencing with chain-terminating inhibitors. *Proc Natl Acad Sci USA* 74(12):5463–5467.
36. Glicklis R, Merchuk JC, Cohen S (2004) Modeling mass transfer in hepatocyte spheroids via cell viability, spheroid size, and hepatocellular functions. *Biotechnol Bioeng* 86(6):672–680.
37. Patolsky F, Zheng G, Lieber CM (2006) Fabrication of silicon nanowire devices for ultrasensitive, label-free, real-time detection of biological and chemical species. *Nat Protoc* 1(4):1711–1724.